PAPER • OPEN ACCESS

Radiometric characterization of a triggered narrow-bandwidth single-photon source and its use for the calibration of silicon single-photon avalanche detectors

View the article online for updates and enhancements.

Radiometric characterization of a triggered narrow-bandwidth single-photon source and its use for the calibration of silicon single-photon avalanche detectors

Hristina Georgieva[1] ![ORCID]**, Marco López**[1]**, Helmuth Hofer**[1]**, Justus Christinck**[1,2]**, Beatrice Rodiek**[1,2]**, Peter Schnauber**[3]**, Arsenty Kaganskiy**[3]**, Tobias Heindel**[3] ![ORCID]**, Sven Rodt**[3]**, Stephan Reitzenstein**[3] ![ORCID] **and Stefan Kück**[1,2]

[1] Physikalisch-Technische Bundesanstalt, Braunschweig, Germany
[2] Laboratory for Emerging Nanometrology, Braunschweig, Germany
[3] Institut für Festkörperphysik, Technische Universität Berlin, Berlin, Germany

E-mail: hristina.georgieva@ptb.de

Abstract

The traceability of measurements of the parameters characterizing single-photon sources, such as photon flux and optical power, paves the way towards their reliable comparison and quantitative evaluation. In this paper, we present an absolute measurement of the optical power of a single-photon source based on an InGaAs quantum dot under pulsed excitation with a calibrated single-photon avalanche diode (SPAD) detector. For this purpose, a single excitonic line of the quantum dot emission with a bandwidth below 0.1 nm was spectrally filtered by using two tilted interference filters. Since high count rates are essential for many metrological applications, we optimized the setup efficiency by combining high overall transmission of the optical components with a geometrical enhancement of the extraction efficiency of a single quantum dot by a monolithic microlens to reach photon fluxes up to $3.7 \cdot 10^5$ photons per second at the SPADs. A relative calibration of two SPAD detectors with a relative standard uncertainty of 0.7% was carried out and verified by the standard calibration method using an attenuated laser. Finally, an Allan deviation analysis was performed giving an optimal averaging time of 92 s for the photon flux.

Keywords: quantum radiometry, quantum metrology, single-photon source, single-photon detector, quantum dot

(Some figures may appear in colour only in the online journal)

1. Introduction

The range of possible implementations of single-photon sources and detectors is rapidly growing. They find application in many quantum optical technologies such as quantum key distribution, quantum-enhanced imaging, quantum computing, quantum metrology and quantum radiometry [1]. Therefore, there is an increasing need to ensure high accuracy

and metrological traceability of measurements in these fields, also for metrology itself.

In quantum metrology, the identity principle guarantees universality and reproducibility of the observed quantum phenomena, whereas the existence of discrete energy states opens the possibility of reaching high resolution in energy [2]. Moreover, energy conservation for transitions between these states enables a direct connection between macroscopic physical units and the fundamental constants by counting single quanta [3]. For example, single-electron transport pumps [4] could be utilized to realize the unit of Ampere by counting the number of transferred elementary charges per time. Similarly, one can make use of the quantization of the electromagnetic radiation to define the optical power by counting photons. The optical power depends only on the photon flux and on the wavelength of the electromagnetic radiation. A possible choice for a detection system are transition edge sensors, whose main advantage is the number-resolving capability, but they suffer from a reduced temporal resolution [5]. The most widely used photon counting devices nowadays, the SPAD detectors, are unable to resolve the photon number. Consequently, for calibration purposes, highest precision can be reached only by ensuring single-photon purity. This means that there has to be exactly one photon per time interval, while every photon should have the same energy. Laser light fulfills the requirement of monochromatic light, but the nature of the Poisson statistics sets a theoretical limit because of the non-zero probability for multiphoton events. This probability can be reduced by decreasing the mean photon number, but at the cost of a substantial vacuum component. On the other hand, single-photon sources based on quantum emitters and on parametric down conversion can in principle reach simultaneously high efficiency and high single-photon purity [6–9].

Different types of quantum emitters have already been investigated, ranging from trapped atoms or ions to color centers in diamond, quantum dots and organic molecules [10, 11], but yet only a few have been metrologically characterized to allow for a quantitative comparison and evaluation in the field of quantum radiometry. For instance, a nitrogen vacancy center in a nanodiamond was found to have a total photon flux of approx. $2.6 \cdot 10^5$ photons per second and a $g^{(2)}(0)$ value of 0.1 at room temperature; however, its spectral radiant flux was below 350 aW nm^{-1} due to the broad emission spectrum [12]. The first direct detection efficiency calibration of a SPAD detector at a specific wavelength was achieved by using a single organic dye molecule as a light source with a tunable optical radiant flux in the range from 36.5 fW to 334 fW, measured with an analog reference low-noise detector, and a $g^{(2)}(0)$ value below 0.1 [13]. The bright narrow-bandwidth emission at (785.6 ± 0.1) nm was obtained at 3 K via continuous wave pumping. Therefore, the smallest time interval between two consecutive photons Δt_{min} is given by the inverse decay rate of the excited state. A more sophisticated approach would be to use pulsed excitation, so that the time interval is determined by $\Delta t_{min} = 1/f$, where f is the laser repetition frequency—an external parameter that could be used to tune the temporal properties of the single-photon source, as it was

carried out for a silicon vacancy center based single-photon source [14].

In this paper, we present the absolute characterization of semiconductor quantum dots (QDs) under pulsed excitation and their direct application for the relative calibration of two SPAD detectors. The exciton recombination lines of InGaAs QDs under non-resonant excitation have typical linewidths of less than 100 µeV [15, 16] (corresponding to 70 pm at 930 nm) and even reach the Fourier transform limited homogenous linewidth under resonant excitation [17], and hence fulfill the condition of nearly monochromatic radiation. Moreover, their mechanical robustness and conformity with other semiconductor devices, enabling on-chip operation, give them an important advantage over molecule- and nanoparticle-based sources. Furthermore, InGaAs QDs are an important platform for the field of quantum key distribution [18] and allow for the generation of polarization-entangled photons via the biexciton-exciton radiative cascade [19].

2. Single-photon source

The single-photon emitter consists of an InGaAs QD deterministically embedded into a monolithic microlens, positioned on top of a distributed Bragg reflector (see figure 1(a)). Numerical simulations of a similar geometrical configuration [20] predict an enhancement of the extraction efficiency of up to 23%, when using a collecting lens with a numerical aperture (NA) of 0.7. An additional antireflection layer on top of the microlens surface further decreases the coupling losses. The fabrication process is described in detail in reference [21].

The confocal setup, shown in figure 1(b), has a simple and compact design, optimized to reach high transmission at 930 nm. It consists of a self-made confocal microscope with implemented spectral filtering. Bearing in mind that only the actual signal arriving at the detector area is of any relevance for calibrations, we treat the whole system comprised of a quantum emitter and optics for spatial and spectral filtering as a self-contained single-photon source. A diode laser (PicoQuant, LDH-D-C-850), which either operates in continuous wave mode or in pulsed mode with repetition frequencies between 1 kHz and 80 MHz and a pulse width of about 64 ps (full width at half maximum (FWHM)) is used for non-resonant excitation of the QD. The laser beam is reflected at a dichroic beam splitter (Semrock, 875 nm edge Bright-Line) and focused on the sample, which is placed in a helium flow cryostat to maintain a constant temperature of approximately 10 K. The QD fluorescence is collected by an infinity corrected objective (Mitutoyo, 100x Plan Apo NIR HR, NA = 0.7). The fluorescent light passes through one long-pass and two bandpass filters and is then coupled into a single mode (9 µm core diameter) or a multimode (62.5 µm core diameter) optical fiber serving as a pinhole for confocal imaging. The optical fiber can be connected either to a spectrometer, a SPAD detector or a fiber-based Hanbury Brown and Twiss interferometer (HBTI) to analyze the spectral characteristics, measure the photon flux or determine the single-photon purity. For micro-photoluminescence scans, the position of objective 1 is
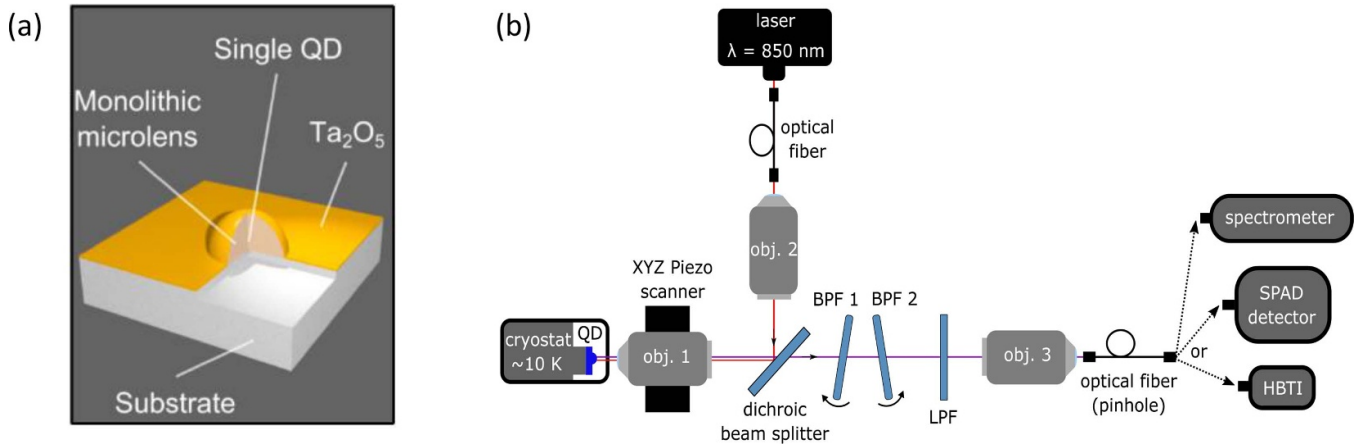
Figure 1. (a) Single InGaAs QD positioned in the center of a monolithic microlens, covered with an antireflection coating to improve the extraction efficiency into the first lens of the setup. Taken from [21]. (b) Experimental setup for the optical characterization of InGaAs QDs emitting in the near infrared.

varied in steps of 0.1 μm via an XYZ piezo scanner and only emission above 900 nm reaches the SPAD detector (Perkin Elmer, SPCM-AQRH-13-FC) due to the long-pass filtering.

In the case of non-resonant excitation, the selection of a spectral line corresponding to the recombination of a specific excitonic state is conventionally carried out by a monochromator, which guarantees high spectral resolution at the cost of polarization dependent transmission and rather high optical losses. Instead, we are using two identical narrow bandpass filters (Alluxa, 935.0–0.45 OD5), based on thin film interference with a transmission of about 90% each (see figures 2(c) and (d)). The FWHM of the transmission window was determined to be 0.5 nm by using a spectrophotometer with a spectral bandwidth of 0.05 nm. For a required wavelength λ_c, defined as the central wavelength of the filter's transmission window, the incident angle θ has to be [22]:

$$\theta = \arcsin\left(\frac{n}{\lambda_0}\sqrt{\lambda_0^2 - \lambda_c^2}\right), \tag{1}$$

where n is the effective refractive index and $\lambda_0 = \lambda_c\,(\theta = 0)$. Both filters are mounted on rotation stages enabling a precise rotation in steps of 100 μrad. The stages are rotated by about the same angle θ in opposite directions to compensate for the angle dependent beam shift (figure 2(a)). A rotation up to 20° completely covers the relevant sample fluorescence range from 915 nm to 935 nm, as shown in figure 2(b).

The overall setup transmission was measured by coupling the monochromatic emission (FWHM = 0.1 nm) of a tunable laser to the optical fiber next to objective 3 and replacing the cryostat by a silicon photodiode. The output power of the laser was monitored to correct for any temporal variations. The transmission of the cryostat window was subsequently added to the overall result, yielding $T_{\text{setup}} = (25.9 \pm 0.4)\,\%$ at (923.1 ± 0.1) nm $(\theta = 15°)$.

The total efficiency depends not only on the wavelength dependent transmission of all optical components, but also
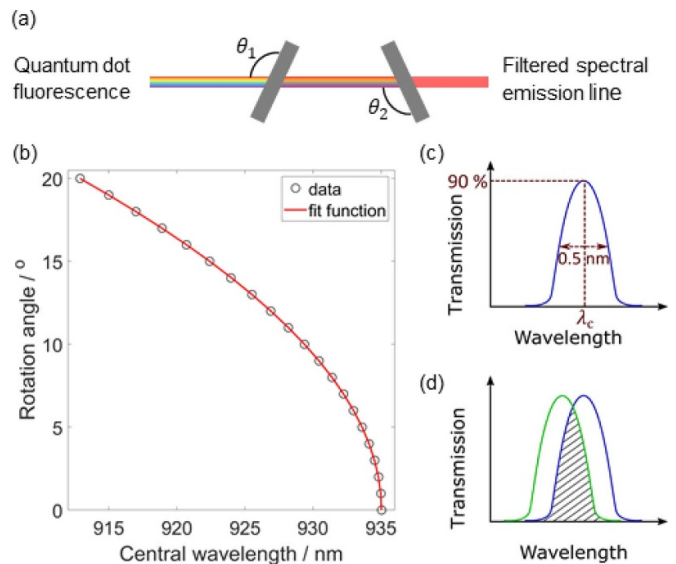

Figure 2. Bandpass filters. (a) Sketch of the spectral filtering with two narrow bandpass filters, tilted by about the same angle in opposite directions. (b) Measurement of the angle dependent blue shift of the transmission window. The red curve shows a good fit of equation (1) to the experimental data. (c) Sketch of the transmission spectrum of a single bandpass filter. (d) Sketch of the spectral overlap of two bandpass filters, denoted by the striped area.

on further dependencies which we currently cannot investigate independently with our setup. For example, the unknown complex intensity profile of the emitter has a strong influence on the extraction efficiency into the first lens, as well as on the coupling efficiency into the optical fiber. A non-zero beam divergence could also lead to optical losses due the high directional sensitivity of the bandpass filters. Furthermore, a non-ideal internal quantum efficiency of the QD and the excitation probability for a specific excitonic transition also play an important role.

For a precise and reliable photon flux determination, the detection efficiency $\eta_{\text{detection}}$ of a SPAD is calibrated against a
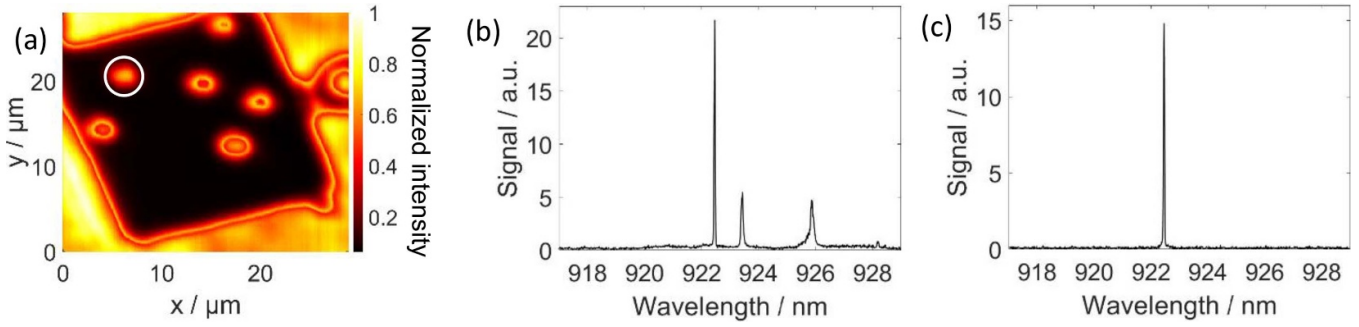
Figure 3. (a) 2D micro-photoluminescence scan of the QD-microlens sample at 10 K. Six deterministically fabricated QD-microlenses are identified by bright emission spots. (b) Spectrum of the emission of the white circled QD-microlens in panel (a) under non-resonant excitation. (c) Emission spectrum after spectral filtering by bandpass interference filters.

reference analog detector by means of the double attenuator technique [23]. Therefore, the absolute photon flux φ and thus the absolute optical power P are traceable to the primary standard for optical power, the cryogenic radiometer.

$$P = \varphi \cdot \frac{hc}{\lambda}, \ \varphi = \frac{\dot{N}_{\mathrm{measured}}}{\eta_{\mathrm{detection}}}. \tag{2}$$

With the redefinition of the SI units from May 2019, the Planck constant h and the speed of light c have exact values with no uncertainties. The narrow bandwidth of the quantum dot spectral lines leads to a small uncertainty for the wavelength λ (about 0.01%). Hence, the main uncertainty contribution comes from the measured photon flux $\dot{N}_{\mathrm{measured}}$. An Allan deviation analysis is conducted to determine the optimal averaging time leading to lowest standard uncertainty.

3. Metrological characterization of the single-photon source

The emission of the QDs embedded into individual monolithic microlenses is spatially and spectrally filtered with the confocal setup shown in figure 1(b) (see previous section). A 2D micro-photoluminescence scan of the QD layer showing the sample emission above 900 nm is used to precisely determine the position of each deterministically fabricated QD-microlens. For the reminder of this work, we choose the QD-microlens marked in figure 3(a), since it simultaneously fulfills the selection criteria of having high brightness as well as high spectral and single-photon purity. The very low signal intensity inside the square region is due to the removal of all QDs and the associated wetting layer between the microlenses by reactive ion etching as part of the fabrication process. Furthermore, the large distance between neighboring QD-microlenses on the order of 5 µm facilitates the convenient spatial selection of a single QD for spectral analysis. A typical spectrum for continuous wave excitation below saturation is presented in figure 3(b). The emission line at (922.4 ± 0.1) nm is filtered by tilting the bandpass filters by angles of $\theta_1 = 15.05°$ and $\theta_2 = 14.95°$, respectively. The absence of any spectral features and background signal in figure 3(c) demonstrates the successful spectral filtering of a single excitonic transition. The FWHM of the spectral peak
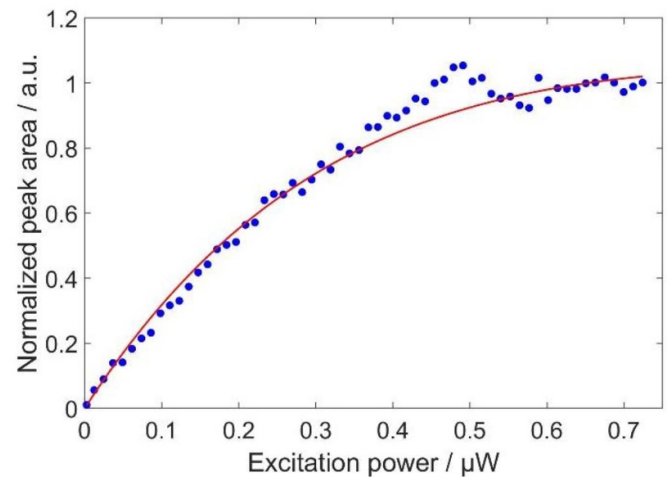

Figure 4. Saturation curve showing the dependence of the area of the spectral peak from figure 3(c) on the mean optical power of the excitation laser. The model from equation (3) for the emission rate of a ground state exciton (red curve) describes well the experimental data.

is determined to be 42 pm and is limited by the spectrometer's resolution.

For a weak excitation, the linear dependence of the normalized peak area on the pump power in figure 4 indicates the recombination of a neutral or a charged exciton. The solution of a system of rate equations [24, 25] describing the photon emission rate of the exciton ground state is given by

$$f(x) = \frac{k_3}{1 + \frac{1}{k_1 x} + k_2 x}. \tag{3}$$

The fit parameters k_1 and k_2 are proportional to the exciton and biexciton radiative lifetimes τ^{X} and τ^{XX}, whereas k_3 is a normalization constant. The variable x represents the exciton creation rate and is thus proportional to the optical power of the excitation laser. Equation (3) is fitted to the data set under the assumption $k_1/k_2 = \tau^{\mathrm{X}}/\tau^{\mathrm{XX}} = 1.8$ [26] and by using the fit parameters $k_2 = (0.78 \pm 0.07) \ \mu\mathrm{W}^{-1}$ and $k_3 = 2.6 \pm 0.1$.

Next, the second-order correlation function $g_{a,b}^{(2)}$ was measured under pulsed excitation with a repetition frequency of
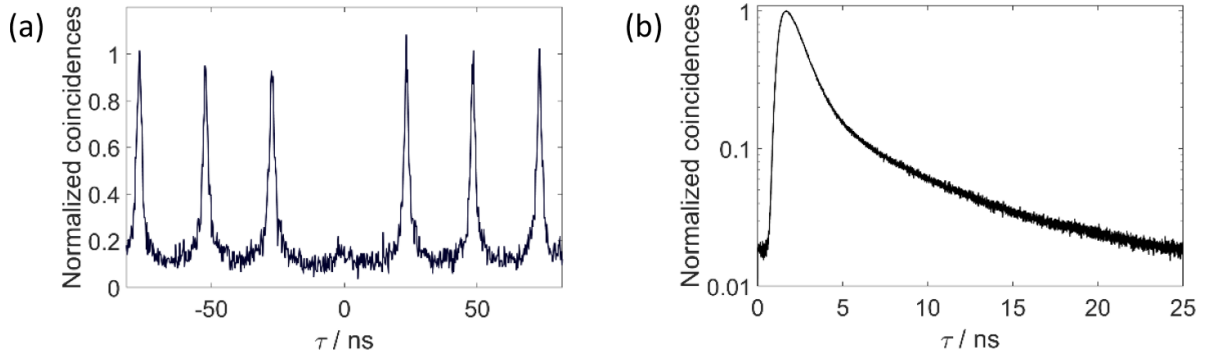
Figure 5. Coincidence histograms for non-resonant pulsed excitation with a repetition frequency of 40 MHz. (a) Second-order correlation measurement (raw data) showing a probability of 0.24 for multiphoton events, when corrected for dark counts. (b) Double exponential exciton decay with decay constants of $(1.11+\text{-}0.02)$ ns and (8.2 ± 0.7) ns.

40 MHz using an HBTI with an overall temporal resolution of 1 ns. The raw data is shown in figure 5(a). This measurement is a result of the detection of two uncorrelated sources with intensities a and b, where a arises from the investigated source and b from the dark counts of the detection system, i.e. when the excitation laser is switched off. The dark counts are assumed to follow Poisson statistics and are completely uncorrelated from the sample emission, i.e. $g_b^2 = 1$. The function $g_{a,b}^{(2)}$ can be expressed as [27, 28]

$$g_{a,b}^{(2)} = \frac{g_a^{(2)} r^2 + 2r + 1}{(r+1)^2}, \quad \text{where } r = \frac{a}{b} \quad (4)$$

and $g_a^{(2)}$ is the dark-count corrected intensity correlation function of the source. The value for $g_{a,b}^{(2)}$ is calculated by binning the coincidences in a time window of 10.5 ns (corresponding to 41 bins), centered at $\tau = n/f_{rep}$, where n is an integer, and dividing the area of the central peak at $\tau = 0$ by the mean area of the six nearest peaks. This yields $g_{a,b}^{(2)}(0) = 0.35 \pm 0.02$ and $g_a^{(2)}(0) = 0.24 \pm 0.06$. There is a constant offset of about 0.1 in the normalized coincidence histogram, considerably affecting the $g^{(2)}(0)$ value. Its origin can be evaluated by a decay rate measurement, presented in figure 5(b). It shows a histogram of the exciton decay for the same excitation repetition frequency of 40 MHz. After 12.5 ns, corresponding to half the repetition period, the signal drops to 3.8%. The decay can be best described by a double exponential function with decay constants of (1.11 ± 0.02) ns and (8.2 ± 0.7) ns and a constant offset of 0.8%. The uncertainties are determined from a comparison of measurements at laser repetition frequencies of 20 MHz, 40 MHz and 80 MHz. A decay time on the order of 1 ns is typical for this type of QDs [29], whereas the second slow decay component creates a peak overlap, which can partially explain the observed offset in figure 5(a). This slow component could be caused by additional dark exciton transitions [30] or by a re-excitation due to a hole recapture process taking place at crystal defects or fluctuations of the wetting layer potential [31].

Another background contribution, that could be observed mainly in the intensity correlation histogram because of the significantly smaller coincidence rate, is fluorescent emission

Table 1. Measured count rates for two different excitation powers and the corresponding absolute values for the photon flux φ and the optical power P, calculated according to equation (2). The detection efficiency $\eta_{\text{detection}}$ was determined by a calibration traceable to the cryogenic radiometer.

Mean excitation power / nW	31.3	219.3
$\dot{N}_{\text{measured}}$ / 10^3 s^{-1}	23.9	119.9
$\eta_{\text{detection}}$ / %	32.6	32.5
φ / 10^3 s^{-1}	73.2	368.6
P / fW	15.8	79.4
Standard uncertainty of P / %	3.4	1.5

from the sample matrix, e.g. from the carrier-overloaded wetting layer. It causes an increasing $g^{(2)}(0)$ value at higher excitation intensities. Since this is an inherent property of the non-resonant excitation, exploiting other excitation schemes (e.g. p-shell and s-shell resonant excitation) is expected to further reduce the value.

The last step of the source characterization is to determine the photon flux and the optical power according to equation (2) (see table 1). The highest optical power amounts to (79.4 ± 1.2) fW. Considering the spectral width of 42 pm, one can calculate a maximum spectral radiant flux of about 1.9 pW nm^{-1} for an excitation rate of 80 MHz.

4. Detection efficiency calibration of Si-SPAD detectors—method

The ratio of detection efficiencies of two commercial silicon SPAD detectors (Perkin Elmer, SPCM-AQRH-13-FC) is determined by using the emission of a single InGaAs QD as a light source. The applied fiber exchange technique is well-known in the field of optical telecommunications [32] and has been successfully implemented for a relative SPAD calibration using the spectrally filtered emission of a nitrogen vacancy center in nanodiamond; however, with count rates below 3000 counts per second and a spectral bandwidth of 19 nm [33]. The model presented here is extended to take into account further systematic deviations.

The spatially and spectrally filtered QD emission is split by a 50:50 fiber-based beam splitter, as shown in figure 6. For the
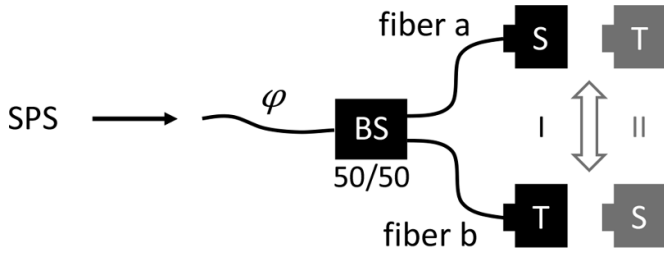
Figure 6. Sketch of the experimental configuration for relative SPAD calibrations according to the fiber exchange technique. The setup consists of a 50/50 beam splitter (BS), connected to two SPAD detectors: standard detector (S) and device under test (T). The photon flux of a single-photon source (SPS) is measured simultaneously with both detectors and the measurement is repeated after detector exchange.

first measurement (*I*), fibers a and b are connected via FC/PC couplers to the standard detector (S) and the device under test (T), respectively. The electrical signal from both detectors is integrated over a period of one second by two counters, synchronized by an external trigger with a frequency of 0.5 Hz. The dark-count corrected counts per second $\dot{N} = \dot{N}_{\text{measured}} - \dot{N}_{\text{dark}}$ for each detector can be expressed as a product of the incoming photon flux φ, the fiber transmission κ and the detection efficiency η: $\dot{N}_{\text{S,a}}^{I} = \varphi^{I} \cdot \kappa_{\text{a}}^{I} \cdot \eta_{\text{S}}$, $\dot{N}_{\text{T,b}}^{I} = \varphi^{I} \cdot \kappa_{\text{b}}^{I} \cdot \eta_{\text{T}}$. For the second measurement (*II*), the positions of the detectors are switched, so that $\dot{N}_{\text{S,b}}^{II} = \varphi^{II} \cdot \kappa_{\text{b}}^{II} \cdot \eta_{\text{S}}$, $\dot{N}_{\text{T,a}}^{II} = \varphi^{II} \cdot \kappa_{\text{a}}^{II} \cdot \eta_{\text{T}}$. The following formula for the ratio *r* of the detection efficiencies can be derived from these four equations:

$$r = \frac{\eta_{\text{S}}}{\eta_{\text{T}}} = \sqrt{\frac{\dot{N}_{\text{S,a}}^{I}}{\dot{N}_{\text{T,b}}^{I}} \cdot \frac{\dot{N}_{\text{S,b}}^{II}}{\dot{N}_{\text{T,a}}^{II}}} \cdot f_{\text{SR}}, \quad f_{\text{SR}} = \sqrt{\frac{\kappa_{\text{b}}^{I}}{\kappa_{\text{b}}^{II}} \cdot \frac{\kappa_{\text{a}}^{II}}{\kappa_{\text{a}}^{I}}} = \sqrt{\frac{SR^{II}}{SR^{I}}}. \quad (5)$$

Consequently, the value of *r* is independent of the incident photon flux and of the splitting ratio *SR* itself, but it depends in general on the variation of this ratio over the course of several measurement series, taken into account by the factor f_{SR}, with $f_{\text{SR}} = 1 \pm u(f_{\text{SR}})$. The uncertainty $u(f_{\text{SR}})$ is set equal to the measured standard deviation of the splitting ratio (SR_{meas}). However, the variations of *SR* cannot be directly decoupled from those of the incoming photon flux, since $SR_{\text{meas}} = \varphi^{I}/\varphi^{II} \cdot SR$, but the temporal stability of φ can be estimated from two consecutive measurement series in each of the two detector configurations.

5. Detection efficiency calibration of Si-SPAD detectors—result

The detection efficiency ratio *r* was determined from ten independent measurement series (see figure 7). Each of them is conducted with a photon flux of approx. $1.2 \cdot 10^5$ photons per second (about $2 \cdot 10^4$ counts per second at each detector), originating from a single spectral line of the QD emission spectrum. This photon flux corresponds to an optical power of 26 fW, being well in the linear regime of the silicon SPAD
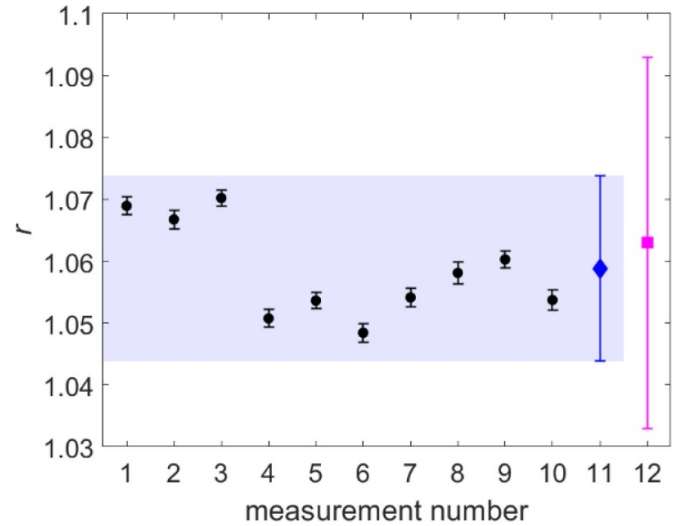

Figure 7. Results of the relative SPAD calibration. Detection efficiency ratios of ten independent measurement series and their type A uncertainties are plotted in black. The blue diamond represents the weighted mean of 1.059 with a total expanded uncertainty (*k* = 2) of 0.015, which includes the type B uncertainty, arising mainly from variations of the splitting ratio. For comparison, the purple square shows the detection efficiency ratio determined by direct calibrations of both SPAD detectors with attenuated laser light.

detectors. Therefore, no attenuation is required, allowing us to achieve a lower overall uncertainty.

The black error bars in figure 7 display the type A uncertainties, which vary between 0.12% and 0.17%. They originate from the statistical variations of 30 measurements per data point. These ten data points are combined into a single value of $r = 1.059$ by taking the weighted mean, whereas their uncertainties are combined by calculating the external consistency, also known as the Birge ratio [34], resulting in a total type A uncertainty of 0.24%.

The discrepancy of the data points is clearly due to an additional uncertainty contribution, most probably due to variations of the splitting ratio, which are accounted for by the factor f_{SR} in equation (5). Changes of the splitting ratio can be caused by insufficient reproducibility of the coupling losses for both connector pairs upon each detector exchange. The relative mean temporal deviation of the incoming photon flux was measured to be 0.30%. Although this contribution has no effect on the uncertainty budget, its value shows a possible overestimation of the type B uncertainty, which amounts to $u(f_{\text{SR}}) = 0.67\%$. All values in figure 7 lie within the total expanded uncertainty (*k* = 2) denoted by the blue area.

One can estimate the expected impact of multiphoton emission from the quantum dot on the detection efficiency calibration. Let p_n be the probability of *n* photons arriving simultaneously at the detection area. In the limit $p_2 \gg p_3, p_4, p_5, \dots$ the $g^{(2)}(0)$ value can be expessed as $g^{(2)}(0) \approx \frac{2p_2}{n^2}$ [35], where $\langle n \rangle \approx 0 \cdot p_0 + 1 \cdot p_1 + 2 \cdot p_2$ is the mean photon number, which differs from the measured value $\langle n_{\text{measured}} \rangle = \varphi/f$ by the factor $\langle n_{\text{measured}} \rangle = \langle n \rangle \cdot (1 - \epsilon)$ due to multiphoton events. The relative correction ϵ when using a non-photon number

resolving detector would be given by the number of not counted photons per pulse divided by the mean photon number:

$$\epsilon = \frac{\sum_{i=1}^{\infty}(i-1)p_i}{\langle n \rangle} \approx \frac{p_2}{\langle n \rangle} \approx \frac{1}{2} \cdot g^{(2)}(0) \cdot \langle n \rangle \qquad (6)$$

The only physically reasonable solution gives an estimated correction of $\epsilon = 0.009\%$, which is significantly smaller than the relative standard uncertainty of 0.7% for the calibration.

Additionally, an absolute detection efficiency calibration method [23] using attenuated laser light (PicoQuant, LDH-D-C-930) at 930 nm was applied to verify the measurement results yielding $\eta_S = 0.327$ and $\eta_T = 0.307$ with a relative standard uncertainty of 1%. To ensure comparability, both calibration methods are applied for the same pulse repetition frequency of 80 MHz, count rate of approx. $2 \cdot 10^4$ counts per second and a fiber core diameter of 62.5 μm. The ratios $r_{QD} = 1.059 \pm 0.008$ and $r_{laser} = 1.063 \pm 0.015$ from both independent methods are in very good agreement within the stated uncertainty, see figure 7. It should be noted that the spectral mismatch of 7.6 nm between laser emission and QD emission leads to an estimated correction by 0.002, which is negligible compared to the standard uncertainties.

6. Count rate stability analysis

The Allan deviation was found to be a very useful tool not only for quantifying the frequency stability of oscillators, but also for stability analysis of an arbitrary signal in the time domain. For example, it has been used for the characterization of gyroscopes [36], microwave radiometers [37], direct current nanovoltmeters [38], SPAD detectors [39] and others. Here, it is used to investigate the temporal stability of the photon flux. The optical signal is split by a 1:2 coupler in order to investigate the dependence of the noise amplitude on the light intensity. The count rate stemming from the QD emission was monitored over a period of seven hours (see figure 8). An increase of signal fluctuations is observed with increasing count rate. The lack of any significant change of the count rates during the whole measurement period demonstrates the stability of the quantum emitter and of the experimental setup.

We are applying the Overlapping Allan deviation (OADEV) [40] because of the improved confidence interval compared to the standard method due to the use of overlapping time intervals. The OADEV $\sigma_y(\tau)$ is a function of the averaging time $\tau = m \cdot \tau_0$, where τ_0 is the basic measurement interval of one second and *m* is an averaging factor. The calculation for *M* measurements with a count rate y_i is done according to the following equation [41]:

$$\sigma_y^2(\tau) = \frac{1}{2m^2(M-2m+1)} \sum_{j=1}^{M-2m+1} \left[\sum_{i=j}^{j+m-1} (y_{i+m} - y_i) \right]^2. \qquad (7)$$

The relative OADEV expressed as a percentage of the mean count rate is presented in figure 9. The counts measured from both SPAD detectors have almost identical values for the relative deviation for averaging times between 1 s and 1500 s
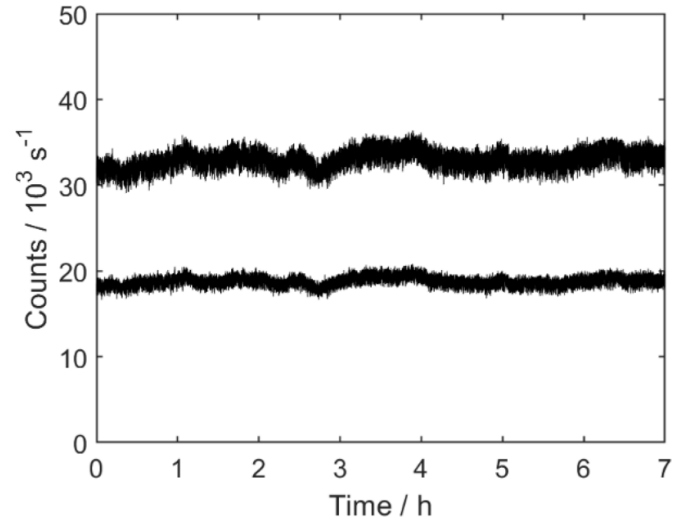

Figure 8. Count rates of the QD emission simultaneously recorded over 7 h with two SPAD detectors positioned behind a fiber-based beam splitter: $1.88 \cdot 10^4$ s^{-1} for SPAD 1 and $3.31 \cdot 10^4$ s^{-1} for SPAD 2.

(blue and red triangles in figure 9), which means that all dominating noise contributions within this time interval scale with the mean value of the count rate. The main noise source is expected to stem from the quantum nature of light; fluctuations of the photon number in a light beam with constant intensity follow the Poisson law [42] and manifest as a shot noise of the electric current upon the electrical conversion of the optical signal by the detection system [43]. Given the fact that the signal-to-noise ratio of the Poisson distribution goes as the square root of the mean photon number, the measurement uncertainty could be further reduced by using a brighter single-photon source.

There is additional intrinsic shot noise originating from the fluctuations of the dark count rate, whose mean value can be determined precisely and subtracted, but its corresponding noise contribution still must be taken into account. For this measurement, it is expected to comprise about 10% of the total shot noise, since the dark counts amount to 207 s^{-1} for SPAD 1 and 333 s^{-1} for SPAD 2.

Another possible noise type arises from the thermal energy of the current carriers and is known as Johnson noise [42]. Both the shot and Johnson noise exhibit no frequency dependence and have a slope of -0.5 [38] in the double logarithmic Allan deviation plot (see figure 9). These seem to be the dominating noise contributions for integration times below 20 s, where the slope has a measured value of -0.44. Then the curve starts to flatten out and reaches its minimum at 92 s. Therefore, this is the optimal averaging time with the smallest achievable uncertainty of 0.58%. The increase of the deviation towards even longer integration times with a slope of 0.40 can be partially explained by a random walk with an expected slope of 0.5 [37]. The low frequency quasi-random fluctuations can have many origins, e.g. a drift in the optical power of the pump laser or in the cryostat temperature. Therefore, the laser power and the
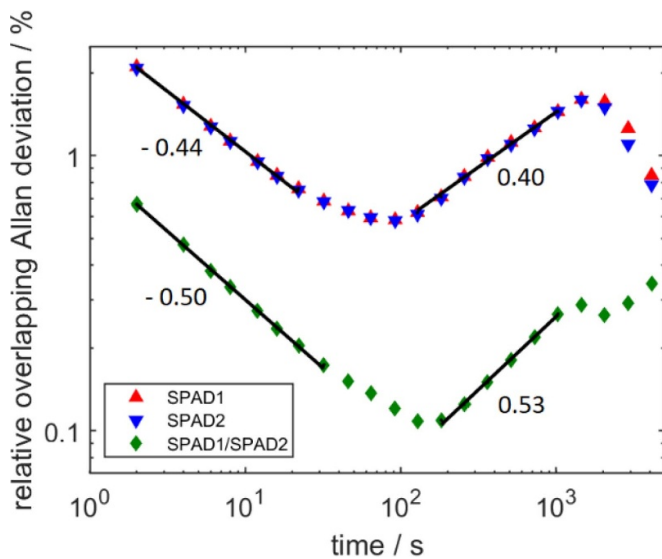
Figure 9. Double logarithmic plot of the relative overlapping Allan deviation for the measured count rate from SPAD 1 (red triangles pointing up), SPAD 2 (blue triangles pointing down) and for the ratio of both count rates (green diamond symbol). The black lines represent fitted slopes to the data points to estimate the dominating noise sources at different averaging times. A minimum deviation of the count rate of 0.6% is reached for a 92 s averaging interval. The count rate ratio can be more precisely determined with a minimum deviation of only 0.1%.

cryostat temperature were monitored during the measurement, yielding correlation coefficients of −0.08 and −0.10 correspondingly. The lack of significant correlation implies that the laser power and temperature shifts of 13 nW and 0.1 K within 7 h have a negligible effect on the count rate stability.

Another possible explanation for the fluctuations on a time scale above 90 s are mechanical instabilities of the optical setup, as slight changes in the position of the objective relative to the quantum emitter would lead to a substantial decrease of the collected light intensity. Additionally, the slight temperature gradient of 0.014 K per hour may induce a mechanical strain in the cryostat, causing a non-linear displacement affecting the collected light intensity. Such a non-linear dependence would not be reflected in the corresponding correlation coefficient.

Of particular interest for the signal stability of the relative calibration method is the OADEV of the ratio of the simultaneously measured count rates of both SPAD detectors (data points marked with diamonds in figure 9). The slope of-0.50 for averaging times below 32 s implies the presence of white noise. A minimum deviation of 0.11% is reached at an averaging time of 128 s. Consequently, the ratio of count rates can be determined with a 5 times better statistical uncertainty compared to the count rate from a single SPAD, since the noise contributions of the simultaneously measured count rates partially cancel out. Responsible for this behavior is their strong correlation (correlation coefficient of 0.95) due to the direct linear dependence of the count rates on the source intensity.

7. Conclusion

A traceable single-photon source based on a non-resonantly driven InGaAs QD with a spectral bandwidth of 42 pm (FWHM) and a single-photon purity corresponding to a $g^{(2)}(0)$ value of 0.24 ± 0.06 was presented. The highest optical power under non-resonant pulsed excitation with a repetition frequency of 80 MHz amounts to (79.4 ± 1.2) fW for an emission wavelength of 922.4 nm. High optical power is achieved by extraction efficiency enhancement through monolithic microlenses and by low loss bandpass filtering, leading to a high setup transmission of $(25.9 \pm 0.4)\%$. The photon flux stability of the source was analysed using the overlapping Allan deviation. Here, white noise dominates for short sampling times and a minimum deviation of 0.58% is reached for averaging 92 values, each with an integration period of 1 s.

This is the first absolutely characterized quantum dot based single-photon source emitting photons under pulsed excitation. The triggered emission enables full control over the time interval between two consecutive photons, which can be used to tune the photon flux over a wide range without changing the saturation properties. Furthermore, we have demonstrated the feasibility of detector calibrations in the near infrared. The ratio of detection efficiencies of two similar SPAD detectors has been determined with a standard uncertainty of 0.7%. This result has been confirmed with the standard double attenuator technique.

The simultaneous count rate measurement as part of the relative calibration allows for reaching statistical uncertainties as low as 0.11% due to the lack of dependence on the temporal stability of the photon flux. Moreover, the count rate ratio does not depend on the brightness of the single-photon source, as long as a sufficient signal-to-noise ratio can be reached.

ORCID iDs

Hristina Georgieva
https://orcid.org/0000-0002-5539-0013
Tobias Heindel
https://orcid.org/0000-0003-1148-404X

Stephan Reitzenstein

https://orcid.org/0000-0002-1381-9838

References

[1] Chunnilall C J, Degiovanni I P, Kück S, Müller I and Sinclair A G 2014 Metrology of single-photon sources and detectors: a review *Opt. Eng.* **53** 081910

[2] Ramsey N F 1995 Quantum mechanics and precision measurements *Phys. Scr.* **T59** 26–28

[3] Göbel E O and Siegner U 2015 *Quantum Metrology: Foundation of Units and Measurements* (Weinheim: Wiley-VCH)

[4] Kaestner B *et al* 2008 Single-parameter nonadiabatic quantized charge pumping *Phys. Rev. B* **77** 153301

[5] von Helversen M, Böhm J, Schmidt M, Gschrey M, Schulze J-H, Strittmatter A, Rodt S, Beyer J, Heindel T and Reitzenstein S 2019 Quantum metrology of solid-state single-photon sources using photon-number-resolving detectors *New J. Phys.* **21** 035007

[6] Liu J *et al* 2019 A solid-state source of strongly entangled photon pairs with high brightness and indistinguishability *Nat. Nanotechnol.* **14** 586–93

[7] Wang H *et al* 2019 On-demand semiconductor source of entangled photons which simultaneously has high fidelity, efficiency, and indistinguishability *Phys. Rev. Lett.* **122** 113602

[8] Fischbach S *et al* 2017 Single quantum dot with microlens and 3D-printed micro-objective as integrated bright single-photon source *ACS Photonics* **4** 1327–32

[9] Ngah L A, Alibart O, Labonté L, D'Auria V and Tanzilli S 2015 Ultra-fast heralded single photon source based on telecom technology *Laser Photon. Rev.* **9** L1–5

[10] Scheel S 2009 Single-photon sources-an introduction *J. Mod. Opt.* **56** 141–60

[11] Eisaman M D, Fan J, Migdall A and Polyakov S V 2011 Invited review article: single-photon sources and detectors *Rev. Sci. Instrum.* **82** 071101

[12] Rodiek B *et al* 2017 Experimental realization of an absolute single-photon source based on a single nitrogen vacancy center in a nanodiamond *Optica* **4** 71–76

[13] Lombardi P, Trapuzzano M, Colautti M, Margheri G, Degiovanni I P, López M, Kück S and Toninelli C 2019 A molecule-based single-photon source applied in quantum radiometry *Adv. Quantum Technol.* **3** 1900083

[14] Vaigu A, Porrovecchio G, Chu X-L, Lindner S, Smid M, Manninen A, Becher C, Sandoghdar V, Götzinger S and Ikonen E 2017 Experimental demonstration of a predictable single photon source with variable photon flux *Metrologia* **54** 218–23

[15] Leosson K, Jensen J R, Hvam J M and Langbein W 2000 Linewidth statistics of single InGaAs quantum dot photoluminescence lines *Phys. Status Solidi* b **221** 49–53

[16] Skiba-Szymanska J *et al* 2011 Narrow emission linewidths of positioned InAs quantum dots grown on pre-patterned GaAs(100) substrates *Nanotechnology* **22** 065302

[17] Kuhlmann A V, Prechtel J H, Houel J, Ludwig A, Reuter D, Wieck A D and Warburton R J 2015 Transform-limited single photons from a single quantum dot *Nat. Commun.* **6** 8204

[18] Kupko T, von Helversen M, Rickert L, Schulze J-H, Strittmatter A, Gschrey M, Rodt S, Reitzenstein S and Heindel T 2020 Tools for the performance optimization of single-photon quantum key distribution *Npj Quantum Inf.* **6** 29

[19] Benson O, Santori C, Pelton M and Yamamoto Y 2000 Regulated and entangled photons from a single quantum dot *Phys. Rev. Lett.* **84** 2513–6

[20] Gschrey M *et al* 2015 Highly indistinguishable photons from deterministic quantum-dot microlenses utilizing three-dimensional in situ electron-beam lithography *Nat. Commun.* **6** 7662

[21] Schnauber P *et al* 2016 Bright single-photon sources based on anti-reflection coated deterministic quantum dot microlenses *Technologies* **4** 1

[22] Smith W J 1990 *Modern Optical Engineering: The Design of Optical Systems* 2nd edn (New York: McGraw-Hill)

[23] López M, Hofer H and Kück S 2015 Detection efficiency calibration of single-photon silicon avalanche photodiodes traceable using double attenuator technique *J. Mod. Opt.* **62** 1732–8

[24] Dekel E, Gershoni D, Ehrenfreund E, Garcia J M and Petroff P M 2000 Carrier-carrier correlations in an optically excited single semiconductor quantum dot *Phys. Rev. B* **61** 11009–20

[25] Kamada H, Ando H, Temmyo J and Tamamura T 1998 Excited-state optical transitions of excitons and biexcitons in a single $In_xGa_{1-x}As$ quantum disk *Phys. Rev. B* **58** 16243–51

[26] Wimmer M, Nair S V and Shumway J 2006 Biexciton recombination rates in self-assembled quantum dots *Phys. Rev. B* **73** 165305

[27] Schell A W, Kaschke J, Fischer J, Henze R, Wolters J, Wegener M and Benson O 2013 Three-dimensional quantum photonic elements based on single nitrogen vacancy-centers in laser-written microstructures *Sci. Rep.* **3** 1577

[28] Brouri R, Beveratos A, Poizat J-P and Grangier P 2000 Photon antibunching in the fluorescence of individual color centers in diamond *Opt. Lett.* **25** 1294–6

[29] Becher C, Kiraz A, Michler P, Imamoğlu A, Schoenfeld W V, Petroff P M, Zhang L and Hu E 2001 Nonclassical radiation from a single self-assembled InAs quantum dot *Phys. Rev. B* **63** 121312

[30] Dalgarno P A, Smith J M, Gerardot B D, Govorov A O, Karrai K, Petroff P M and Warburton R J 2005 Dark exciton decay dynamics of a semiconductor quantum dot *Phys. Status Solidi* a **202** 2591–7

[31] Dalgarno P A, McFarlane J, Brunner D, Lambert R W, Gerardot B D, Warburton R J, Karrai K, Badolato A and Petroff P M 2008 Hole recapture limited single photon generation from a single n-type charge-tunable quantum dot *Appl. Phys. Lett.* **92** 193103

[32] Hofer H, López M and Kück S 2008 Fiber-based power measurements for the optical telecommunication in a wide spectral range *10th Int. Conf. on New Developments and Applications in Optical Radiometry* pp 105–6

[33] Schmunk W, Rodenberger M, Peters S, Hofer H and Kück S 2011 Radiometric calibration of single photon detectors by a single photon source based on NV-centers in diamond *J. Mod. Opt.* **58** 1252–9

[34] Birge R T 1932 The calculation of errors by the method of least squares *Phys. Rev.* **40** 207–27

[35] Schmunk W *et al* 2012 Photon number statistics of NV centre emission *Metrologia* **49** 156–60

[36] El-Sheimy N, Hou H and Niu X 2008 Analysis and modeling of inertial sensors using Allan variance *IEEE Trans. Instrum. Meas.* **57** 140–9

[37] Land D V, Levick A P and Hand J W 2007 The use of the Allan deviation for the measurement of the noise and drift performance of microwave radiometers *Meas. Sci. Technol.* **18** 1917–28

[38] Witt T J 2001 Using the Allan variance and power spectral density to characterize DC nanovoltmeters *IEEE Trans. Instrum. Meas.* **50** 445–8

[39] Lunghi T, Korzh B, Sanguinetti B and Zbinden H 2014
Absolute calibration of fiber-coupled single-photon detector
Opt. Express **22** 18078–92

[40] Snyder J J 1981 An ultra-high resolution frequency meter
Thirty Fifth Annual Frequency Control Symp. pp
464–9

[41] Riley W J 2008 NIST Special Publication: *Handbook of
Frequency Stability Analysis* (Washington: U.S.
Government Printing office)

[42] Bell D A 1960 *Electrical Noise: Fundamentals and Physical
Mechanism* (London: Van Nostrand)

[43] Blum A 1996 *Elektronisches Rauschen* (Stuttgart: Teubner)